

Mechanism-driven CO₂ Capture and Activation on Two-dimensional Transition-metal Diborides

Jakkapat Seeyangnok^{1a}, Rungkiat Nganglumpoon²,
 Joongjai Panpranot^{2b}, Udomsilp Pinsook^{1b}

¹Department of Physics, Faculty of Science,
 Chulalongkorn University, Bangkok, Thailand

^ajakkapatjtp@gmail.com

^bjoongjai.p@chula.ac.th

^cUdomsilp.P@chula.ac.th

Abstract

The urgent need to mitigate rising atmospheric CO₂ levels motivates the search for stable, efficient, and tunable adsorbent materials. In this study, we employ first-principles density functional theory to investigate the adsorption of CO₂ molecules on two-dimensional hexagonal transition-metal diboride monolayers, M₂B₂ (M = Sc, Y, Ti, Zr, Nb). The adsorption energies, structural distortions, and bonding characteristics are systematically analyzed to understand how the metal center governs CO₂ activation. The calculated adsorption energies range from -1.84 to -2.16 eV (or -1.98 to -4.42), with Ti₂B₂ and Sc₂B₂ exhibiting the strongest CO₂ binding, while Y₂B₂, Zr₂B₂, and Nb₂B₂ show moderately strong chemisorption. Adsorption induces significant molecular activation, evidenced by elongated C–O bonds (1.27–1.29 Å) and bent O–C–O angles (129–132°), compared to the linear gas-phase configuration (1.17 Å, 180°). Charge analysis further reveals substantial electron transfer from the monolayer to CO₂^{δ-}, consistent with strong chemisorption and structural deformation. Correspondingly, the shift toward less negative IpCOHP(E_f) values indicates a pronounced weakening of the internal C–O bonds, reflecting increased population of antibonding π^* orbitals. Ab initio molecular dynamics simulations show that the activated CO₂^{δ-} species is thermally sensitive: while most M₂B₂ surfaces retain stable adsorption at 300 K, Ti₂B₂ drives spontaneous CO₂ dissociation into CO and O, revealing a temperature-assisted activation pathway. These findings highlight how the choice of transition metal tunes electronic interactions, adsorption energetics, and activation pathways on M₂B₂ surfaces. Overall, this work identifies two-dimensional transition-metal diborides as promising candidates for next-generation CO₂ capture and activation technologies.

Keywords: CO₂ capture; two-dimensional materials; transition-metal diborides; charge transfer; surface activation

1 Introduction

Global temperature records extending back to the late 19th century reveal a persistent warming trend. NASA’s Goddard Institute for Space Studies (GISS) recognized this increase as early as the 1980s, and their most recent analyses report a global temperature rise of more than 0.8 °C since 1951 [1,2]. Over the past century, human activities have driven a substantial increase in the emission of greenhouse gases, with carbon dioxide identified as the most significant contributor. Atmospheric CO₂ concentrations continue

to rise steadily each year, increasing from 313 ppm in 1960 to more than 425 ppm in 2025 [3]. This rapid escalation in CO₂ levels has become one of the most pressing environmental challenges of our time. The efficient capture and conversion of greenhouse gases, particularly CO₂, are therefore central to global climate-mitigation strategies and ecosystem protection efforts. Developing stable, efficient materials for CO₂ capture [4,5] remains a major scientific and technological challenge, as practical deployment requires a combination of high adsorption capacity, selectivity, and long-term chemical robustness. Despite significant advances in adsorption-, absorption-, and membrane-based separation technologies [6, 7], many available CO₂ sorbents still face limitations such as low selectivity, high regeneration costs, degradation under working conditions, or insufficient binding strength. These persistent drawbacks emphasize the ongoing need for new classes of materials with improved CO₂ affinity, tunable surface reactivity, and long-term stability under realistic industrial and environmental conditions [8, 9].

Two-dimensional (2D) materials have emerged as promising platforms for gas capture [10–12] and surface-driven chemical processes owing to their large surface areas, exposed active sites, and tunable electronic properties. Considerable progress has been made on systems such as transition-metal dichalcogenides (TMDs), whose structural, electronic, and chemical properties have been widely reviewed [13, 14], and which also exhibit highly reactive hydrogenated surfaces [15–20] including Li functionalization [21, 22]. These characteristics have enabled TMDs to demonstrate strong potential in gas capture and sensing applications [23, 24]. MXenes, another major family of 2D materials, have similarly been extensively investigated for their surface chemistry and functional versatility [25, 26]. Their surfaces also undergo hydrogenation [27, 28], halogen functionalization [29] and numerous studies have demonstrated their suitability for CO₂ capture and separation [23, 30–33]. Hexagonal boron nitride (h-BN), known for its chemical stability and tunable adsorption characteristics [34], has likewise shown promising gas adsorption behavior [35]. More recently, boron-based 2D analogues such as BXenes have been predicted and reviewed as emerging materials with unique bonding characteristics [36, 37], and initial investigations indicate their potential for CO₂ capture [38].

These diverse families of 2D materials exhibit rich surface chemistry and offer valuable opportunities for designing efficient CO₂ adsorption and activation pathways at the atomic scale. Within this expanding landscape, 2D transition-metal borides have gained increasing attention as a new class of ultrathin materials characterized by robust structural stability and highly reactive surfaces [37, 39]. In particular, hexagonal M₂B₂ monolayers have emerged as promising candidates for a wide range of applications. Several studies have explored their potential for metal-ion battery technologies [40–45], highlighting their favorable electronic and structural characteristics. Moreover, many hexagonal M₂B₂ BXene monolayers exhibit exceptionally active surfaces, as demonstrated by their strong tendency toward surface hydrogenation [46–48], which has also been linked to enhanced superconducting behavior [47, 48]. This pronounced surface reactivity suggests that these materials may also serve as efficient platforms for CO₂ capture, activation, and conversion. Despite these promising attributes, however, the adsorption behavior and surface chemistry of CO₂ on hexagonal M₂B₂ BXenes remain largely unexplored.

Given the global need for effective strategies to mitigate CO₂ emissions, identifying new materials capable of stable and selective CO₂ adsorption is of significant interest. In this work, we use first-principles calculations to investigate the structural, electronic, and surface chemical properties of hexagonal M₂B₂ (M = Sc, Y, Ti, Zr, Nb) monolayers and their interactions with CO₂. We first evaluate the geometry, phase stability, formation energies, and mechanical and dynamical robustness of the pristine monolayers to establish their viability as free-standing 2D materials. We then examine CO₂ adsorption by determining the most favorable binding configurations and analyzing the associated adsorption energetics and molecular distortions. To elucidate the adsorption mechanism, we investigate charge redistribution and bonding characteristics using Löwdin and Bader charge analysis and Crystal Orbital Hamilton Population (COHP) calculations. These results provide fundamental insight into the surface reactivity of this

emerging class of 2D transition-metal borides and underscore their potential for CO₂ capture and related catalytic applications.

2 Methods

The structural and electronic properties of the M₂B₂ monolayers (M = Sc, Y, Ti, Zr, Nb) were investigated using density functional theory (DFT) as implemented in QUANTUM ESPRESSO [49, 50]. Initial structures were generated in VESTA [51] and optimized with the BFGS quasi-Newton scheme [52, 53] until the residual atomic forces were below 10⁻⁵ eV/Å. A vacuum spacing of 20 Å was applied along the out-of-plane direction to avoid interactions between periodic images. Exchange–correlation effects were described using the GGA-PBE functional [54] and PAW pseudopotentials [55]. Plane-wave cutoffs of 60 Ry (wavefunctions) and 240 Ry (charge density) were used. Brillouin-zone sampling employed a 21 × 21 × 1 Monkhorst–Pack grid [56] with a first-order Methfessel–Paxton smearing of 0.02 Ry [55].

For the CO₂ adsorption calculations, a 3 × 3 × 1 supercell of the M₂B₂ monolayers was employed together with a 7 × 7 × 1 *k*-point mesh to ensure convergence of total energies and adsorption geometries. Long-range dispersion interactions, which play a non-negligible role in molecule–surface binding, were accounted for using Grimme’s D3 correction [57]. To further investigate the bonding characteristics and surface chemical reactivity toward CO₂, Crystal Orbital Hamilton Population (COHP) analyses were performed using the *LOBSTER* code [58–60].

The interaction strength between CO₂ and the M₂B₂ (M = Sc, Y, Ti, Zr, Nb) monolayers was assessed through the adsorption energy, E_{absorp} , which quantifies the energetic preference for CO₂ binding. It is expressed as

$$E_{\text{absorp}} = E_{\text{M}_2\text{B}_2+\text{CO}_2} - (E_{\text{M}_2\text{B}_2} + E_{\text{CO}_2}), \quad (1)$$

where $E_{\text{M}_2\text{B}_2+\text{CO}_2}$ denotes the total energy of the relaxed CO₂–M₂B₂ complex, $E_{\text{M}_2\text{B}_2}$ is the energy of the isolated monolayer, and E_{CO_2} corresponds to the energy of a free CO₂ molecule calculated in vacuum. A negative value of E_{absorp} signifies that the adsorption process is exothermic and thus thermodynamically favorable.

3 Results and discussion

3.1 Crystal structure and stability of hexagonal M₂B₂ monolayers

The optimized atomic structures of two-dimensional hexagonal M₂B₂ (M = Sc, Y, Ti, Zr, Nb) monolayers are illustrated in Figure 1. Each structure adopts a hexagonal primitive cell (Bravais lattice type: hP) with the extended Bravais symbol hP2 and belongs to the space group *P6/mmm* (No. 191), indicating a highly symmetric planar configuration with inversion symmetry. In the optimized geometry within the *xy* plane, two boron atoms occupy the fractional coordinates (0.3333, 0.6667) and (0.6667, 0.3333), forming a characteristic honeycomb network, while the metal atom is located at (0.0000, 0.0000), residing at the center of the boron hexagon. The calculated lattice constants are summarized in Table 1.

We also examined the magnetic characteristics of the hexagonal M₂B₂ (M = Sc, Y, Ti, Zr, Nb) BXene monolayers by initializing the systems in several distinct spin configurations. First, a ferromagnetic (FM) state was imposed by assigning parallel magnetic moments to all metal atoms. In addition, two antiferromagnetic (AFM) arrangements were explored: a G-type pattern, where each metal site is set to oppose the spin of all its nearest neighbors, and an A-type pattern, in which the spins within the lower

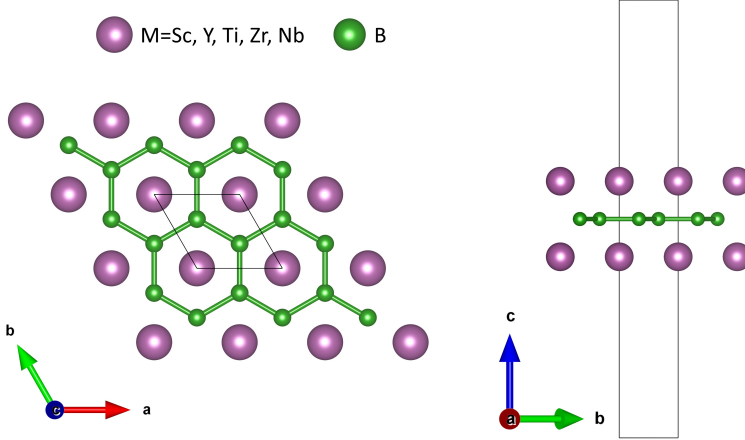


Figure 1: Top (left) and side (right) views of the optimized atomic structure of two-dimensional hexagonal M_2B_2 ($M = \text{Sc, Y, Ti, Zr, Nb}$) monolayer. The purple and green spheres represent the metal (M) and boron (B) atoms, respectively. The black lines indicate the primitive unit cell. The structure exhibits a planar boron honeycomb layer sandwiched between two metal atom layers.

M layer are aligned while those in the upper layer are reversed. Independent of the initial spin ordering, the hexagonal M_2B_2 BXene monolayers consistently relax into a metallic ground state.

Table 1: Optimized lattice constants a and metal–metal layer thickness h_M of the hexagonal M_2B_2 monolayers.

M_2B_2 monolayer	a (Å)	h_M (Å)
Sc_2B_2	3.12	3.46
Y_2B_2	3.29	3.76
Ti_2B_2	3.00	3.12
Zr_2B_2	3.16	3.38
Nb_2B_2	3.10	3.05

The electronic structure of the hexagonal M_2B_2 monolayers is metallic, with states near the Fermi level predominantly derived from the transition-metal d -orbital manifold. At the Γ point, these d states split into well-defined symmetry groups: the A' state originating from the d_{z^2} orbital, the E' states from the in-plane d_{xy} and $d_{x^2-y^2}$ orbitals, and the E'' states from the out-of-plane d_{yz} and d_{xz} orbitals. The substantial d -orbital contribution at the Fermi level indicates a high density of available surface electrons, which can strongly influence adsorbate–surface interactions. This electronic configuration is therefore expected to facilitate charge transfer and enhance the activation of CO_2 upon adsorption.

The dynamical stability of the two-dimensional M_2B_2 ($M = \text{Sc, Y, Ti, Zr, Nb}$) monolayers was examined by calculating their phonon dispersion relations using density functional perturbation theory. The phonon spectra for all systems show no imaginary (negative) frequencies throughout the entire Brillouin zone as shown in Figure 2, confirming that each M_2B_2 structure is dynamically stable which corresponds to previous studies [40–48]. In particular, the acoustic modes near the Γ point exhibit the expected quadratic behavior for the out-of-plane (ZA) mode and linear dispersions for the in-plane (LA and TA) modes, characteristic of stable two-dimensional materials.

To further investigate the lattice dynamical behavior, the phonon eigenvalues and eigenvectors at the Γ point were extracted and are summarized in Table 2 and Figure 3, respectively. The highest-frequency optical modes originate predominantly from vibrations of the boron sublattice ($E1u$, $A2u$, $B1g$, and $E2g$), spanning a range of 365.7 – 926.7 cm $^{-1}$. In contrast, the transition-metal atoms dominate the low-frequency region, corresponding to the $E1g$ and $A1g$ modes, which lie between 164.8 and 284.4 cm $^{-1}$ across the series of transition metals. The high-frequency boron-related modes are a direct consequence

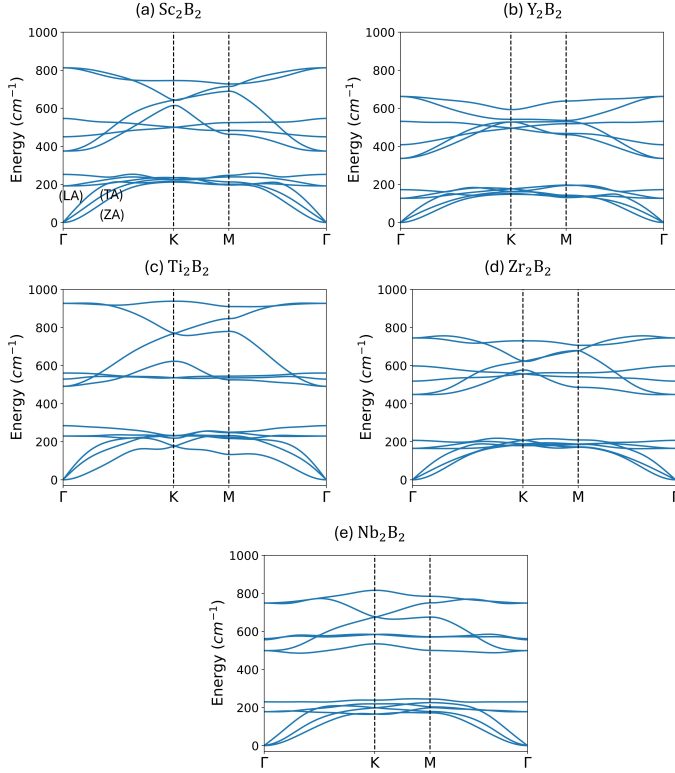


Figure 2: Phonon dispersion relations of the pristine two-dimensional M_2B_2 ($M = \text{Sc}, \text{Y}, \text{Ti}, \text{Zr}, \text{Nb}$) monolayers along the high-symmetry path Γ –K–M– Γ in the Brillouin zone. Panels (a)–(e) correspond to Sc_2B_2 , Y_2B_2 , Ti_2B_2 , Zr_2B_2 , and Nb_2B_2 , respectively. The absence of imaginary phonon modes confirms the dynamic stability of all $M_2\text{B}_2$ monolayers.

Table 2: Selected optical phonon vibrational modes (in cm^{-1}) and their symmetry representations for pristine $M_2\text{B}_2$ ($M = \text{Sc}, \text{Y}, \text{Ti}, \text{Zr}, \text{Nb}$) monolayers. Raman-active (R) and infrared-active (I) modes are indicated.

Modes	Sc_2B_2	Y_2B_2	Ti_2B_2	Zr_2B_2	Nb_2B_2
E_{1g} (R)	191.4	126.6	230.2	164.8	178.1
A_{1g} (R)	252.5	172.5	284.4	207.1	229.9
E_{1u} (I)	365.7	339.5	500.3	440.1	490.9
A_{2u} (I)	454.5	414.0	535.9	523.7	565.5
B_{1g}	546.6	531.2	560.7	598.2	561.9
E_{2g} (R)	812.8	662.2	926.7	745.1	749.0

of the strong B–B bonding network, suggested by earlier findings [48].

3.2 Adsorption energetics and surface reactivity

Figure 4 presents the optimized adsorption configurations of CO_2 molecules on the surfaces of two-dimensional $M_2\text{B}_2$ ($M = \text{Sc}, \text{Y}, \text{Ti}, \text{Zr}, \text{Nb}$) monolayers, shown from both top and side views. In all cases, the CO_2 molecule interacts directly with the metal site, indicating that the transition-metal atoms. The CO_2 molecule undergoes noticeable bending upon adsorption, suggesting partial activation due to charge transfer between the molecule and the substrate. This behavior demonstrates the chemisorptive nature of the interaction rather than weak physisorption. The bending angle of CO_2 are particularly sensitive to the metal type, with lighter elements (e.g., Sc and Ti) exhibiting larger molecular distortion compared to heavier elements (e.g., Y, Zr, and Nb).

As summarized in Table 3, the adsorption energies of CO_2 on the $M_2\text{B}_2$ ($M = \text{Sc}, \text{Y}, \text{Ti}, \text{Zr}, \text{Nb}$)

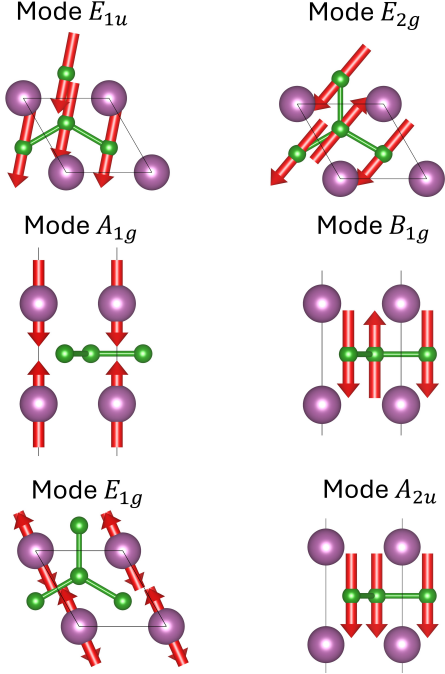


Figure 3: Schematic representation of the zone-center vibrational modes of the hexagonal M_2B_2 monolayers, illustrating the atomic displacement patterns for the symmetry modes E_{1u} , E_{2g} , A_{1g} , B_{1g} , E_{1g} , and A_{2u} . Red arrows indicate the direction and relative magnitude of atomic motions for metal (purple) and boron (green) atoms within each irreducible representation. These modes correspond to the phonon eigenvectors at the Γ point and are used to analyze the vibrational and dynamical stability of the monolayers.

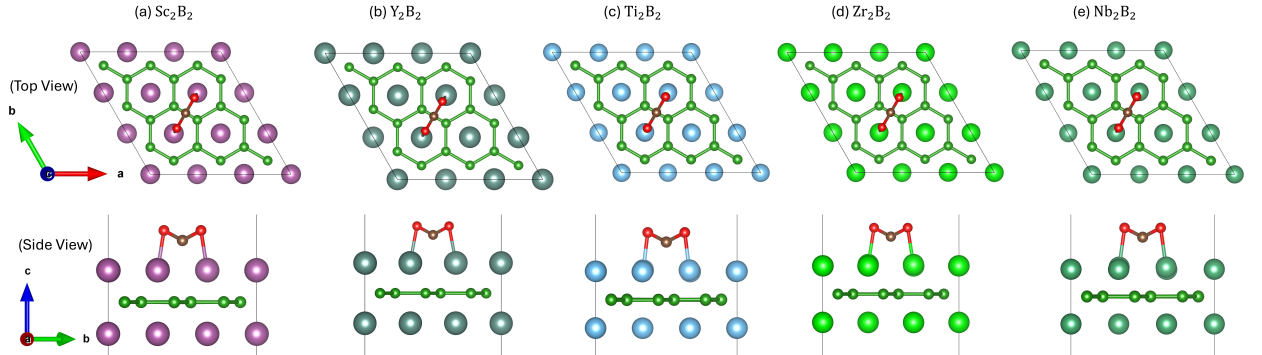


Figure 4: Top (upper panels) and side (lower panels) views of the optimized geometries of CO_2 adsorption on two-dimensional M_2B_2 ($M = Sc, Y, Ti, Zr, Nb$) monolayers: (a) Sc_2B_2 , (b) Y_2B_2 , (c) Ti_2B_2 , (d) Zr_2B_2 , and (e) Nb_2B_2 . The red, brown, green, and colored (purple, dark green, blue, light green, and cyan) spheres represent oxygen, carbon, boron, and metal (M) atoms, respectively. The adsorption configurations show that CO_2 molecules are chemisorbed on the M_2B_2 surfaces with different binding orientations, depending on the type of transition metal.

monolayers reveal strong chemisorption across all systems, with E_{ads} values ranging from -1.84 to -2.16 eV. Among the studied materials, Ti_2B_2 and Sc_2B_2 exhibit the strongest adsorption, with $E_{ads} = -2.16$ eV and -2.15 eV, respectively, while Nb_2B_2 and Zr_2B_2 show slightly weaker but still substantial binding strengths. Concurrently, the CO_2 molecule undergoes significant structural deformation upon adsorption when compared to its isolated configuration. In the gas phase, CO_2 has a C–O bond length of 1.17 Å and a linear O–C–O angle of 180° ; however, upon adsorption, the C–O bonds elongate to 1.27 – 1.29 Å, and the O–C–O angle decreases markedly to approximately 129° – 132° . This pronounced

Table 3: Combined structural, energetic, and electronic characteristics of $\text{CO}_2^{\delta-}$ adsorption on M_2B_2 monolayers. Adsorption energies E_{ads} are in eV; C–O bond lengths d_{CO} are in Å; O–C–O angles are in degrees; lpCOHP(E_f) is in eV; and charge transfer (CT) values are in units of e from Löwdin and Bader analyses.

System	E_{ads} (eV)	d_{CO} (Å)	O–C–O (°)	lpCOHP(E_f) (eV)	Löwdin CT (e)	Bader CT (e)
CO_2 (isolated)	–	1.17	180.00	-18.29	–	–
Sc_2B_2	-2.15	1.28	129.97	-13.98	0.55	1.43
Y_2B_2	-1.93	1.28	129.05	-13.91	0.20	1.46
Ti_2B_2	-2.16	1.29	131.96	-14.16	0.52	1.34
Zr_2B_2	-1.87	1.28	131.05	-14.20	0.13	1.35
Nb_2B_2	-1.84	1.27	132.14	-14.43	0.09	1.17

molecular bending and bond stretching indicate weakening of the C–O bonds and reflect substantial activation of CO_2 on the M_2B_2 surfaces. These structural and energetic trends confirm the chemisorptive nature of the interaction and demonstrate that M_2B_2 monolayers, particularly those containing early transition metals, provide highly reactive platforms capable of promoting CO_2 activation.

3.3 Charge Transfer and Bonding Characteristics

The Löwdin charge analysis [61] further confirms that CO_2 receives a substantial amount of electronic charge upon adsorption on the M_2B_2 monolayers. As shown in Table 3, the total electronic population on the CO_2 molecule increases from 16 electrons in the isolated state to values between approximately 16.09 and 16.55 electrons after adsorption. This corresponds to charge transfer values of $0.55e$, $0.20e$, $0.52e$, $0.13e$, and $0.09e$ for the Sc-, Y-, Ti-, Zr-, and Nb-based systems, respectively. The relatively large charge transfer observed for Sc_2B_2 and Ti_2B_2 correlates with their stronger adsorption energies and the more pronounced structural deformation of the CO_2 molecule, indicating a higher degree of activation. In contrast, the smaller charge transfer in Zr_2B_2 and Nb_2B_2 reflects weaker interaction strength and reduced bending of CO_2 .

The Bader charge analysis [62] as shown in Table 3 also supports this trend, revealing even larger electron transfer to the adsorbed CO_2 molecule. The computed charge transfer values are $1.46e$, $1.43e$, $1.34e$, $1.35e$, and $1.17e$ for the Sc-, Y-, Ti-, Zr-, and Nb-based systems, respectively, indicating that CO_2 is reduced to a $\text{CO}_2^{\delta-}$ species on all M_2B_2 surfaces. Although the absolute values differ from those of the Löwdin scheme due to the distinct charge-partitioning methods, both analyses consistently exhibit the same qualitative trend: early transition-metal borides (Sc and Y) transfer more charge to CO_2 , whereas Nb donates the least. The larger Bader charges in Sc_2B_2 and Y_2B_2 correlate with more severe molecular deformation and stronger activation, while the smaller charge in Nb_2B_2 correlates with weaker distortion and reduced reactivity. Together, the Löwdin and Bader results provide compelling evidence that electron donation from the M_2B_2 surface is the primary driving force for weakening the internal C–O bonds and promoting CO_2 activation.

To further confirm the presence of charge transfer, as suggested by the Löwdin and Bader charge analyses, we analyzed the charge density difference, defined as

$$\Delta\rho = \rho_{\text{M}_2\text{B}_2+\text{CO}_2} - \rho_{\text{M}_2\text{B}_2} - \rho_{\text{CO}_2}, \quad (2)$$

where ρ_{total} denotes the charge density of the combined adsorption system, while ρ_{surface} and ρ_{CO_2} represent the charge densities of the isolated surface and the CO_2 molecule, respectively. The charge density difference $\Delta\rho$ confirms charge transfer from the M_2B_2 surface to the CO_2 molecule, as shown in Fig. 5. This is evidenced by charge accumulation (yellow) on the CO_2 molecule and charge depletion

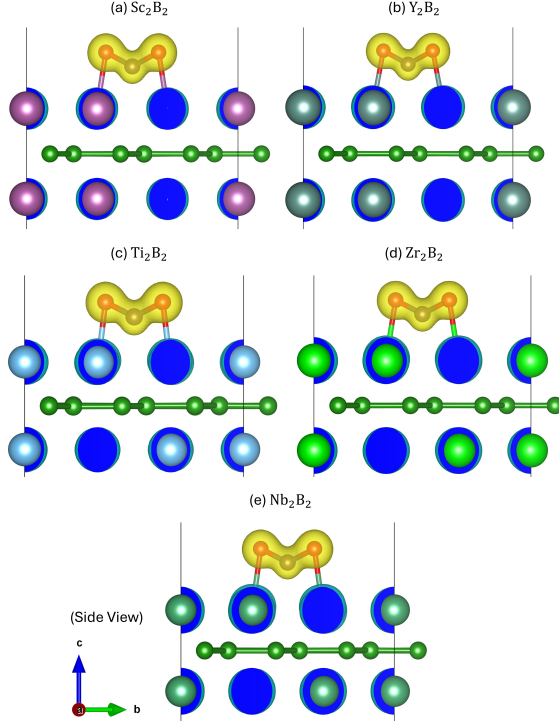


Figure 5: Charge density difference plots for CO_2 adsorption on the surface at an isosurface level of 0.15. Yellow and cyan denote charge accumulation and depletion, respectively, indicating interfacial charge transfer upon adsorption.

(cyan) on the M_2B_2 surface corresponding to the Löwdin and Bader charge analyses.

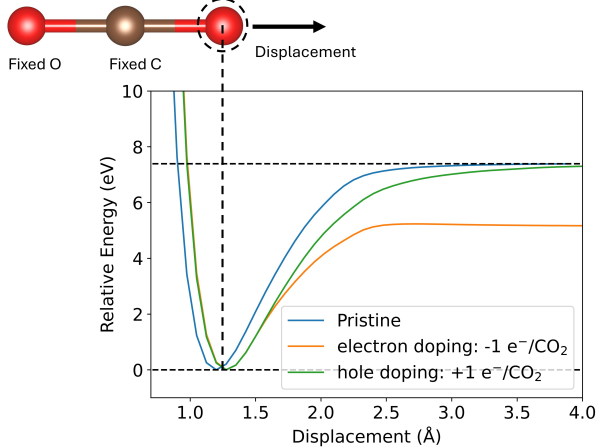


Figure 6: Schematic representation (top) of the constrained desorption pathway, where one oxygen atom and the carbon atom of CO_2 are fixed while the second oxygen atom is displaced away from the adsorption site. The corresponding relative energy profiles (bottom) are shown for pristine, electron-doped ($-1 \text{ e}^-/\text{CO}_2$), and hole-doped ($+1 \text{ e}^-/\text{CO}_2$) M_2B_2 systems as a function of the displacement of the free oxygen atom. Electron doping significantly lowers the desorption energy barrier, making CO_2 easier to detach, whereas hole doping slightly lowers the barrier relative to the pristine system.

The influence of charge transfer on CO_2 bond strength is further reflected in the desorption energy profiles shown in Figure 6. Both electron and hole doping reduce the depth of the potential well relative to pristine CO_2 , but to markedly different degrees. The electron-doped case ($-1 \text{ e}^-/\text{CO}_2$) exhibits the shallowest potential well, indicating that the additional electronic charge most effectively weakens

the internal C–O bonds. Hole doping ($+1\text{ e}^-/\text{CO}_2$) also produces a slightly shallower well than the pristine molecule, though the effect is considerably weaker. This behavior is fully consistent with the adsorption trends observed for the M_2B_2 monolayers: systems such as Sc_2B_2 and Ti_2B_2 , which transfer the largest amount of charge to the adsorbed molecule, induce the strongest CO_2 activation—manifested by pronounced C–O bond elongation, significant bending, and more adsorption energies. In contrast, monolayers that donate less charge, such as Zr_2B_2 and Nb_2B_2 , produce weaker distortions and reduced activation. Thus, the isolated CO_2 desorption curves offer a clear mechanistic interpretation of the structural and energetic trends across the M_2B_2 series: greater electron donation leads to stronger activation and more pronounced weakening of the C–O bonds.

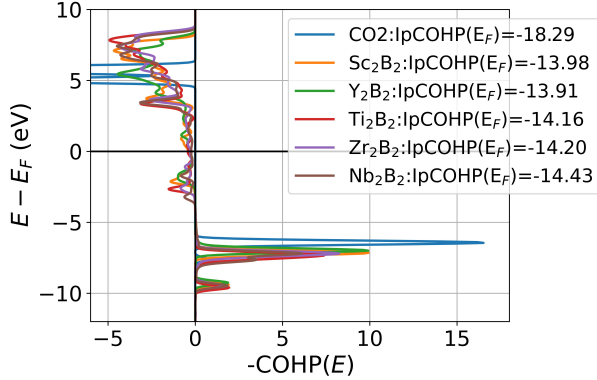


Figure 7: Crystal orbital Hamilton population (COHP) analysis of the C–O bonds in CO_2 for the isolated molecule and for CO_2 adsorbed on the M_2B_2 ($\text{M} = \text{Sc}, \text{Y}, \text{Ti}, \text{Zr}, \text{Nb}$) monolayers. The $-\text{COHP}(E)$ curves are plotted as a function of energy referenced to the Fermi level ($E - E_F$). More negative $\text{IpCOHP}(E_F)$ values correspond to stronger C–O bonding.

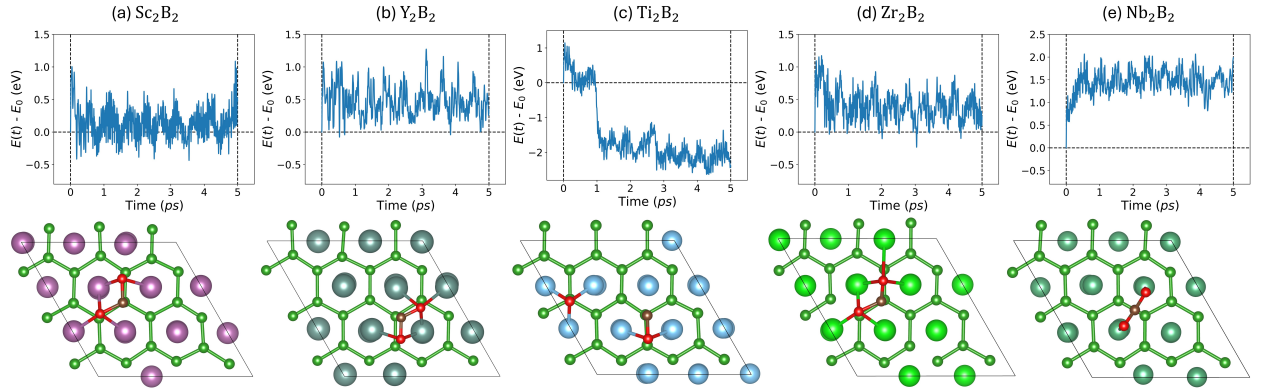


Figure 8: Ab initio molecular dynamics (AIMD) simulations of CO_2 adsorbed on (a) Sc_2B_2 , (b) Y_2B_2 , (c) Ti_2B_2 , (d) Zr_2B_2 , and (e) Nb_2B_2 monolayers at 300 K. Top panels show the time evolution of the total energy relative to the initial value, $E(t) - E_0$, over a 5 ps trajectory, demonstrating thermal stability and the absence of desorption events under ambient conditions. Bottom panels display the final atomic configurations obtained at the end of the AIMD runs (top view).

The crystal orbital Hamilton population (COHP) analysis as shown in Figure 7 provides direct insight into how adsorption on the M_2B_2 monolayers modifies the intrinsic C–O bonding in CO_2 . For isolated CO_2 , the strongly negative $\text{IpCOHP}(E_F)$ value of -18.29 eV reflects the robust covalent character of the C–O double bonds. Upon adsorption, however, the $\text{IpCOHP}(E_F)$ values become substantially less negative, ranging from -13.91 to -14.43 eV as summarized in Table 3. This reduction indicates a pronounced weakening of the internal C–O bonds, consistent with the elongated C–O bond lengths and

bent O–C–O angles obtained from structural optimization. The shift toward less negative $\text{IpCOHP}(E_f)$ values reveals increased population of antibonding π^* orbitals as shown in Figure 7 just below Fermi level, lowering the C–O bond order and transforming the molecule into a chemically activated $\text{CO}_2^{\delta-}$ species.

The trend in COHP results correlates strongly with the amount of electron transfer to CO_2 , as revealed by the Löwdin and Bader charge analyses also listed in Table 3. Systems exhibiting large charge transfer—such as Sc_2B_2 and Ti_2B_2 —show the greatest reductions in $\text{IpCOHP}(E_f)$, reflecting stronger filling of antibonding orbitals and consequently more severe weakening of the C–O bonds. In contrast, Zr_2B_2 and Nb_2B_2 , which transfer significantly less charge, maintain more negative $\text{IpCOHP}(E_f)$ values and exhibit correspondingly less absorption energies. Together, the COHP and charge-transfer results provide a consistent and unified picture: electron donation from the M_2B_2 surface is the primary mechanism responsible for weakening the C–O bonds and driving CO_2 activation across the examined monolayers.

3.4 Thermal Effects on $\text{CO}_2^{\delta-}$ Adsorption

Further investigation of thermal effects was carried out using ab initio molecular dynamics (AIMD) simulations of CO_2 adsorbed on hexagonal M_2B_2 monolayers at 300 K within the NVT ensemble, with the corresponding energy fluctuations and final configurations shown in Figure 8. Interestingly, the AIMD trajectories reveal multiple distinct final configurations, consistent with the structural variations also found in static optimizations performed with different initial CO_2 orientations (see Appendix). These final AIMD results are consistent with the optimized structures obtained from configuration (g), where the CO_2 molecule aligns itself along the boron honeycomb network, leading to the most stable adsorption configuration.

For Nb_2B_2 , the final CO_2 geometry remains essentially unchanged, matching the optimized adsorption structure reported in Figure 4. In contrast, Sc_2B_2 , Y_2B_2 , and Zr_2B_2 exhibit slight re-orientations of the reactive $\text{CO}_2^{\delta-}$ species: although the molecule stays chemisorbed, it realigns itself with the underlying boron network during the simulation. The most pronounced thermal effect occurs for Ti_2B_2 , where one O atom dissociates from the activated $\text{CO}_2^{\delta-}$, resulting in spontaneous cleavage into CO and O fragments at room temperature. These results demonstrate that the activated $\text{CO}_2^{\delta-}$ species is highly sensitive to thermal fluctuations, and that even mild thermal energy at 300 K can significantly rearrange—or fully break—the molecular configuration on the most reactive M_2B_2 surfaces.

4 Conclusion

In this work, we performed a comprehensive first-principles investigation of CO_2 adsorption and activation on hexagonal transition-metal diboride monolayers, M_2B_2 ($\text{M} = \text{Sc}, \text{Y}, \text{Ti}, \text{Zr}, \text{Nb}$), to evaluate their potential as two-dimensional materials for CO_2 capture and surface reactivity. All pristine M_2B_2 monolayers were confirmed to be mechanical, dynamically, and energetically stable. Across the entire series, CO_2 adsorption was found to be strongly exothermic, with adsorption energies in the range of -1.84 to -2.16 eV (or -1.98 to -4.42), reflecting robust chemisorption rather than weak physisorption. This strong interaction induces pronounced structural deformation of the molecule, including elongation of the C–O bonds and bending of the O–C–O angle, signaling significant activation of CO_2 upon binding.

Charge-transfer analyses using Löwdin and Bader schemes consistently revealed substantial electron donation from the M_2B_2 surface to the adsorbed CO_2 , yielding a negatively charged $\text{CO}_2^{\delta-}$ species. Early transition metals ($\text{Sc}, \text{Ti}, \text{Y}$) exhibited the largest charge transfer and correspondingly the strongest adsorption and molecular deformation. These trends were further corroborated by COHP calculations,

which showed a marked decrease in $\text{IpCOHP}(E_f)$ values for the C–O bonds after adsorption. This shift toward less negative $\text{IpCOHP}(E_f)$ indicates enhanced population of antibonding π^* states, leading to significant weakening of the internal C–O bonds—an essential electronic signature of CO_2 activation.

Importantly, ab initio molecular dynamics simulations revealed that the activated $\text{CO}_2^{\delta-}$ species is highly sensitive to thermal fluctuations. At 300 K, the M_2B_2 surfaces exhibited distinct dynamical behavior: Nb_2B_2 retained a stable chemisorbed configuration, while Sc_2B_2 , Y_2B_2 , and Zr_2B_2 showed moderate reorientation of the adsorbed molecule. Notably, Ti_2B_2 induced spontaneous dissociation of $\text{CO}_2^{\delta-}$ into CO and O during the simulation. These results indicate that once CO_2 is activated to a bent, electron-rich $\text{CO}_2^{\delta-}$ form, its weakened C–O bonds become highly susceptible to thermally driven rearrangement or even bond cleavage at room temperature. The optimization of configuration (g) as discussed in The Appendix also show that the

Overall, the combined structural, electronic, and bonding analyses demonstrate that hexagonal M_2B_2 monolayers, particularly those incorporating early transition metals, provide highly reactive platforms capable of activating CO_2 through a charge-transfer-driven mechanism. These findings position two-dimensional transition-metal diborides as promising candidates for future CO_2 capture, activation, and potentially catalytic conversion technologies. The insights established here offer a foundation for rational design and chemical tuning of boride-based 2D materials aimed at advancing next-generation carbon management strategies.

Data Availability

The data that support the findings of this study are available from the corresponding authors upon reasonable request.

Code Availability

The first-principles DFT calculations were performed using the open-source Quantum ESPRESSO package, available at <https://www.quantum-espresso.org>, along with pseudopotentials from the Quantum ESPRESSO pseudopotential library at <https://pseudopotentials.quantum-espresso.org/>.

Acknowledgments

This research project is supported by the Second Century Fund (C2F), Chulalongkorn University. We acknowledge the supporting computing infrastructure provided by NSTDA, CU, CUAASC, NSRF via PMUB [B05F650021, B37G660013] (Thailand).

Author Contributions

Jakkapat Seeyangnok conceptualized the research idea, performed all calculations and visualizations, analyzed the results, and wrote the manuscript. Rungkiat Nganglumpon and Joongjai Panpranot contributed to the analysis and manuscript writing. Udomsilp Pinsook coordinated the project, contributed to the analysis, and edited the final manuscript.

Conflict of Interests

The authors declare no competing financial or non-financial interests.

Appendix

Appendix A: Configurational CO₂ substitutions

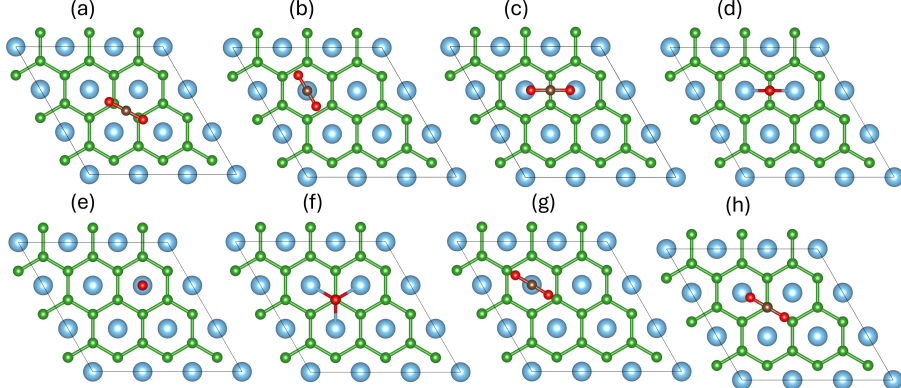


Figure 9: Top-view structures of the considered initial CO₂ adsorption configurations on the hexagonal M₂B₂ monolayer. (a)–(c) and (g)–(h): CO₂ aligned parallel to the M₂B₂ surface at different adsorption sites. (d)–(f): CO₂ aligned vertically relative to the monolayer surface. Green, blue, brown, and red spheres represent B, transition-metal, C, and O atoms, respectively.

To explore the adsorption behavior of CO₂ molecules on the hexagonal M₂B₂ monolayer, various initial adsorption configurations were constructed, as illustrated in Figure 9. These configurations include different adsorption sites (top, bridge, and hollow positions) and molecular orientations. In configurations (d), (e), and (f), the CO₂ molecule is oriented vertically with respect to the M₂B₂ surface, whereas in configurations (a)–(c) and (g)–(h), CO₂ is aligned parallel to the monolayer.

For the vertical adsorption configurations (d), (e), and (f), the CO₂ molecules remain almost upright after structural relaxation, similar to their initial configuration, indicating weak physisorption with relatively small adsorption energies, -0.14 to -1.24 eV, as summarized in Table 4.

Table 4: Adsorption energies (in eV) of CO₂ for configurations (b), (d), (e), (f), (g) and (h) on M₂B₂ monolayers.

Configuration	Sc	Y	Ti	Zr	Nb
(a,c)	-2.15	-1.93	-2.16	-1.87	-1.84
(b)	-1.24	-0.98	-1.05	-0.60	-0.14
(d)	-0.10	-0.13	-0.24	-0.09	-0.10
(e)	-0.21	-1.44	-0.22	-0.20	-0.26
(f)	-0.08	-2.06	-0.26	-0.08	-0.10
(g)	-3.38	-2.22	-4.42	-4.93	-1.98
(h)	-2.26	-2.06	-2.57	-2.15	-3.75

The initial configurations (a) and (c) converge to the same optimized adsorption structure, as shown in Figure 4, which has already been discussed in the main text. Configuration (b) also results in a bent CO₂ geometry after relaxation (Figure 10), indicating partial activation of the molecule. However, as summarized in Table 4, the corresponding adsorption energies of configuration (b) are generally smaller than those of configurations (a) and (c), revealing a weaker interaction with the M₂B₂ surface.

Finally, the initial configurations (g) and (h) lead to very interesting outcomes. For some transition metals, the optimized structures show a dissociation of one O atom from the CO₂ molecule, consistent with the final AIMD result shown in Figure 8(c) for Ti₂B₂. For configuration (g), most systems relax into a similar adsorption geometry to the final MD state, where the CO₂ molecule aligns itself along the boron honeycomb network, as illustrated in Figure 8(a,b,d,e) and Figure 11(a). These optimized

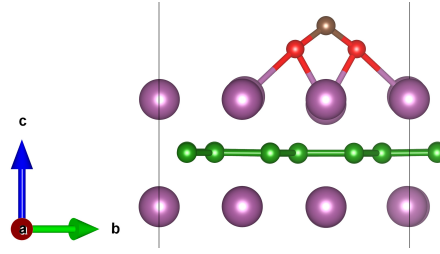


Figure 10: Side-view structure of the CO_2 adsorption configuration (b) on the M_2B_2 monolayer. After relaxation, the CO_2 molecule becomes bent due to the interaction with the surface. Brown, red, green, and purple spheres represent C, O, B, and transition-metal atoms, respectively.

configurations yield even lower adsorption energies ranging from -19.8 to -4.42 eV, as summarized in Table 4, in good agreement with our AIMD results. Interestingly, in the case of Zr_2B_2 , one O atom detaches from CO_2 , indicating a strong chemisorption interaction and partial CO_2 decomposition, as shown in Figure 11.

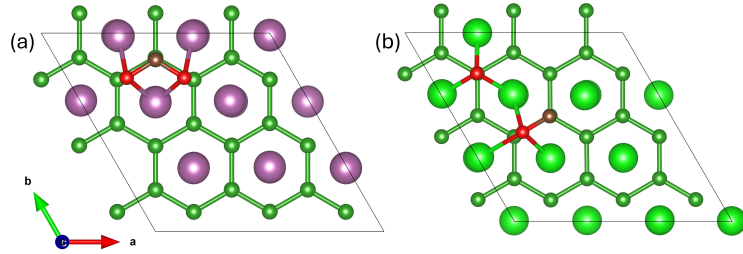


Figure 11: Final optimized adsorption configurations obtained from the initial (g) configuration of CO_2 on M_2B_2 monolayers. Panel (a) shows that the structure converges to the same adsorption geometry for Sc, Y, Ti, and Nb systems. Panel (b) corresponds to the Zr_2B_2 case, where one O atom dissociates from the CO_2 molecule, indicating strong chemisorption and partial CO_2 decomposition. Brown, red, green, and purple spheres represent C, O, B, and transition-metal atoms, respectively.

For configuration (h), the optimized structure is similar to the final configurations obtained from (a) and (b), but with a slightly tilted CO_2 orientation, as shown in Figure 12(a). Interestingly, in the case of Nb_2B_2 , one O atom dissociates from CO_2 , indicating strong chemisorption and partial CO_2 decomposition, as presented in Figure 12(b).

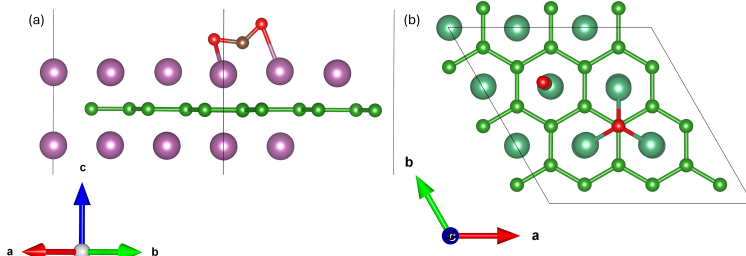


Figure 12: Final optimized adsorption configurations obtained from the initial (h) configuration of CO_2 on M_2B_2 monolayers. (a) Most systems converge to a slightly tilted adsorption geometry similar to those observed in configurations (a) and (b). (b) For Nb_2B_2 , one O atom dissociates from the CO_2 molecule, indicating a strong chemisorption interaction and partial CO_2 decomposition. Brown, red, green, and the larger spheres represent C, O, B, and M atoms, respectively. The lattice vectors (\mathbf{a} , \mathbf{b} , \mathbf{c}) are shown for reference.

References

- [1] James Hansen, Reto Ruedy, Makiko Sato, and Ken Lo. Global surface temperature change. *Reviews of Geophysics*, 48(4), 2010.
- [2] NASA Goddard Institute for Space Studies. Gistemp v4: Global surface temperature analysis (land–ocean temperature index). https://data.giss.nasa.gov/gistemp/graphs_v3/, 2025. Accessed: 2025-11-14.
- [3] NOAA Global Monitoring Laboratory. Trends in atmospheric carbon dioxide (CO₂). <https://gml.noaa.gov/ccgg/trends/>, 2025. Accessed: 2025-11-14.
- [4] Jieyuan Li, Meiling Hou, Yanqiu Chen, Wanglai Cen, Yinghao Chu, and Shi Yin. Enhanced CO₂ capture on graphene via n,s dual doping. *Applied Surface Science*, 399:420–425, 2017.
- [5] Sherif Abdulkader Tawfik, X. Y. Cui, S. P. Ringer, and C. Stampfl. Multiple CO₂ capture in stable metal-doped graphene: A theoretical trend study. *RSC Advances*, 5(63):50975–50982, 2015.
- [6] Cheng-Hsiu Yu, Chih-Hung Huang, and Chung-Sung Tan. A review of CO₂ capture by absorption and adsorption. *Aerosol and Air Quality Research*, 12(5):745–769, 2012.
- [7] Paola A. Saenz Cavazos, Elwin Hunter-Sellars, Paul Iacomi, Sean R. McIntyre, David Danaci, and Daryl R. Williams. Evaluating solid sorbents for CO₂ capture: Linking material properties and process efficiency via adsorption performance. *Frontiers in Energy Research*, 11:1167043, 2023.
- [8] Eloy S. Sanz-Pérez, Christopher R. Murdock, Stephanie A. Didas, and Christopher W. Jones. Direct capture of CO₂ from ambient air. *Chemical Reviews*, 116(19):11840–11876, 2016.
- [9] Matthew E. Boot-Handford, Juan C. Abanades, Edward J. Anthony, Martin J. Blunt, Stefano Brandani, Niall Mac Dowell, José R. Fernández, Maria-Chiara Ferrari, Robert Gross, Jason P. Hallett, et al. Carbon capture and storage update. *Energy & Environmental Science*, 7(1):130–189, 2014.
- [10] Shengxue Yang, Chengbao Jiang, and Su-Huai Wei. Gas sensing in two-dimensional materials. *Applied Physics Reviews*, 4(2), 2017.
- [11] Chandra Prakash, Ankit K. Yadav, Minakshi Sharma, Vijay K. Singh, and Ambesh Dixit. Recent developments on two-dimensional materials for gas sensing applications. *Journal of Physics: Condensed Matter*, 2024.
- [12] Jin Zhou, Chang Wang, Xinhao Zhang, Lin Jiang, and Renbing Wu. Advances in two-dimensional layered materials for gas sensing. *Materials Science and Engineering R: Reports*, 161:100872, 2024.
- [13] Sajedeh Manzeli, Dmitry Ovchinnikov, Diego Pasquier, Oleg V. Yazyev, and Andras Kis. Two-dimensional transition metal dichalcogenides. *Nature Reviews Materials*, 2(8):1–15, 2017.
- [14] Saju Joseph, Jainy Mohan, Seetha Lakshmy, Simil Thomas, Brahmananda Chakraborty, Sabu Thomas, and Nandakumar Kalarikkal. A review of the synthesis, properties, and applications of two-dimensional transition metal dichalcogenides and their heterostructures. *Materials Chemistry and Physics*, 297:127332, 2023.
- [15] Ang-Yu Lu, Hanyu Zhu, Jun Xiao, Chih-Piao Chuu, Yimo Han, Ming-Hui Chiu, Chia-Chin Cheng, Chih-Wen Yang, Kung-Hwa Wei, Yiming Yang, et al. Janus monolayers of transition metal dichalcogenides. *Nature Nanotechnology*, 12(8):744–749, 2017.

- [16] Jakkapat Seeyangnok, M. Munib Ul Hassan, Udomsilp Pinsook, and Graeme Ackland. Superconductivity and electron self-energy in tungsten–sulfur–hydride monolayer. *2D Materials*, 11(2):025020, 2024.
- [17] Jakkapat Seeyangnok, Udomsilp Pinsook, and Graeme J. Ackland. Superconductivity and strain-enhanced phase stability of janus tungsten chalcogenide hydride monolayers. *Physical Review B*, 110(19):195408, 2024.
- [18] Shu-Xiang Qiao, Kai-Yue Jiang, Chang-Hao Sui, Peng-Cheng Xiao, Na Jiao, Hong-Yan Lu, and Ping Zhang. Prediction of charge density wave, superconductivity, and topology in two-dimensional janus 2h/1t-wxh (x = s, se). *Materials Today Physics*, 46:101485, 2024.
- [19] Jakkapat Seeyangnok, Udomsilp Pinsook, and Graeme J. Ackland. Competition between superconductivity and ferromagnetism in two-dimensional janus MXH (m = ti, zr, hf; x = s, se, te) monolayers. *Journal of Alloys and Compounds*, 1033:180900, 2025.
- [20] Akkarach Sukserm, Jakkapat Seeyangnok, and Udomsilp Pinsook. Half-metallic and ferromagnetic phases in CrSH monolayers using DFT+u and BO-md calculations. *Physical Chemistry Chemical Physics*, 27:3950–3959, 2025.
- [21] Hongmei Xie, Zhijing Huang, Yinchang Zhao, Hao Huang, Geng Li, Zonglin Gu, and Shuming Zeng. Strong electron–phonon coupling and multigap superconductivity in 2h/1t janus mosli monolayer. *The Journal of Chemical Physics*, 160(23), 2024.
- [22] Jakkapat Seeyangnok, Udomsilp Pinsook, and Greame John Ackland. Two-gap superconductivity in a janus moseli monolayer. *arXiv preprint arXiv:2412.08119*, 2024.
- [23] Ali Mirzaei, Jin-Young Kim, Hyoun Woo Kim, and Sang Sub Kim. Resistive gas sensors based on two-dimensional TMDs and MXenes. *Accounts of Chemical Research*, 57(16):2395–2413, 2024.
- [24] Eduard Llobet. Transition metal dichalcogenide-based toxic gas sensing. *Current Opinion in Environmental Science & Health*, 37:100533, 2024.
- [25] Xinliang Li, Zhaodong Huang, Christopher E. Shuck, Guojin Liang, Yury Gogotsi, and Chunyi Zhi. MXene chemistry, electrochemistry, and energy storage applications. *Nature Reviews Chemistry*, 6(6):389–404, 2022.
- [26] Raheela Akhter and Shrikant S. Maktedar. MXenes: A comprehensive review of synthesis, properties, and progress in supercapacitor applications. *Journal of Materomics*, 9(6):1196–1241, 2023.
- [27] Jakkapat Seeyangnok and Udomsilp Pinsook. Ab initio investigation on structural stability and phonon-mediated superconductivity in two-dimensional hydrogenated M₂X (M = mo, v, zr; X = c, n) MXene monolayers. *Journal of Physics and Chemistry of Solids*, page 113346, 2025.
- [28] Jakkapat Seeyangnok and Udomsilp Pinsook. Phase stability and superconductivity in hydrogenated and lithiated janus GaXS₂ (X = ga, in) monolayers. *Journal of Applied Physics*, 138(16):164302, 2025.
- [29] Jakkapat Seeyangnok and Udomsilp Pinsook. Enhanced and tunable superconductivity enabled by mechanically stable halogen-functionalized mo₂c mxenes, 2026.
- [30] Jarosław Serafin, Stefanos Chaitoglou, Ghulam Farid, Yang Ma, Bartosz Dziejarski, Adria Sanchez, Xavier Vendrell, and Roger Amade. MXenes: Multifunctional two-dimensional materials for hydrogen evolution, energy storage, and carbon capture applications. *Chemical Engineering Journal*, page 168650, 2025.

[31] Raul Morales-Salvador, Jose D. Gouveia, Angel Morales-Garcia, Francesc Vines, Jose R. B. Gomes, and Francesc Illas. Carbon capture and usage by MXenes. *ACS Catalysis*, 11(17):11248–11255, 2021.

[32] Yuanyuan Wang, Zhenhua Niu, Yangyang Dai, Peng Mu, and Jian Li. Two-dimensional MXene nanomaterials for efficient gas separation: A review. *Nanoscale*, 15(9):4170–4194, 2023.

[33] Mihrimah Ozkan, Thinh Truong, Shirish Pathak, Li-Ren Liu, Francois Dubreuil, and Pushkar Suke. Scaling up carbon capture with robust and stable MXenes for sustainability. *MRS Energy & Sustainability*, pages 1–32, 2025.

[34] Kailiang Zhang, Yulin Feng, Fang Wang, Zhengchun Yang, and John Wang. Two-dimensional hexagonal boron nitride (2D-hBN): Synthesis, properties, and applications. *Journal of Materials Chemistry C*, 5(46):11992–12022, 2017.

[35] Hongyan Guo, Wenhua Zhang, Ning Lu, Zhiwen Zhuo, Xiao Cheng Zeng, Xiaojun Wu, and Jinlong Yang. CO₂ capture on h-BN sheets with high selectivity controlled by external electric field. *The Journal of Physical Chemistry C*, 119(12):6912–6917, 2015.

[36] Mohammad Ramezanzadeh, Reza Ghamarpoor, Ali Dashan, Akram Fallah, Soolmaz Soleimani, and Bahram Ramezanzadeh. Two-dimensional transition metal borides (MBenes): A comprehensive review of the materials, chemistry, advances, and novel applications. *Advanced Composites and Hybrid Materials*, 8(3):269, 2025.

[37] Abdul Jabbar Khan, Syed Shaheen Shah, Shaukat Khan, Abdul Mateen, Bushra Iqbal, Mizna Naseem, Liang He, Yi Zhang, Yong Che, Ya Tang, et al. Two-dimensional metal borides (MBenes): Synthesis methods for energy storage applications. *Chemical Engineering Journal*, 497:154429, 2024.

[38] Siavash Iravani, Atefeh Zarepour, Arezoo Khosravi, and Ali Zarrabi. Environmental and biomedical applications of two-dimensional transition metal borides (MBenes): Recent advancements. *Nanoscale Advances*, 2025.

[39] Showkat H. Mir, Vivek K. Yadav, and Jayant K. Singh. Efficient CO₂ capture and activation on novel two-dimensional transition metal borides. *ACS Applied Materials & Interfaces*, 14(26):29703–29710, 2022.

[40] Guanghui Yuan, Tao Bo, Xiang Qi, Peng-Fei Liu, Zongyu Huang, and Bao-Tian Wang. Monolayer Zr₂B₂: A promising two-dimensional anode material for lithium-ion batteries. *Applied Surface Science*, 480:448–453, 2019.

[41] Qiu He, Zhaohuai Li, Wenshan Xiao, Chengyi Zhang, and Yan Zhao. Computational investigation of two-dimensional 3d/4d hexagonal transition metal borides for metal-ion batteries. *Electrochimica Acta*, 384:138404, 2021.

[42] Shuli Gao, Jinbo Hao, Xinhui Zhang, Long Li, Chunling Zhang, Liyuan Wu, Xiaoguang Ma, Pengfei Lu, and Gang Liu. Two-dimensional transition metal boride Y₂B₂ as a promising anode in lithium-ion and sodium-ion batteries. *Computational Materials Science*, 200:110776, 2021.

[43] Tao Bo, Peng-Fei Liu, Juping Xu, Junrong Zhang, Yuanbo Chen, Olle Eriksson, Fangwei Wang, and Bao-Tian Wang. Hexagonal Ti₂B₂ monolayer: A promising anode material offering high rate capability for lithium-ion and sodium-ion batteries. *Physical Chemistry Chemical Physics*, 20(34):22168–22178, 2018.

[44] Zhiqiang Lu, Yuchong Kang, Yingjie Du, Xiaoyun Ma, Wei Ma, and Jin Zhang. Functionalizing janus-structured Ti_2B_2 unveils exceptional capacity and performance in lithium-ion battery anodes. *Journal of Colloid and Interface Science*, 661:662–670, 2024.

[45] Zheng Dai, Xixi Jia, and Lina Bai. Theoretical prediction of a novel Ti_2B_2 monolayer phase as an outstanding electrode material for lithium/sodium-ion batteries. *ACS Omega*, 10(20):20465–20473, 2025.

[46] Yu-Lin Han et al. Theoretical prediction of superconductivity in two-dimensional hydrogenated metal diborides: M_2B_2H ($M = al, mg, mo, w$). *Physical Review Materials*, 7(11):114802, 2023.

[47] Yu-Lin Han et al. High-temperature superconductivity in two-dimensional hydrogenated titanium diboride: $Ti_2B_2H_4$. *Materials Today Physics*, 30:100954, 2023.

[48] Jakkapat Seeyangnok, Udomsilp Pinsook, and Graeme J. Ackland. High- T_c two-dimensional ambient BCS superconductors in hydrogenated transition-metal borides. *npj 2D Materials and Applications*, 9(1):70, 2025.

[49] Paolo Giannozzi, Stefano Baroni, Nicola Bonini, Matteo Calandra, Roberto Car, Carlo Cavazzoni, Davide Ceresoli, Guido L. Chiarotti, Matteo Cococcioni, Ismaila Dabo, et al. QUANTUM ESPRESSO: A modular and open-source software project for quantum simulations of materials. *Journal of Physics: Condensed Matter*, 21(39):395502, 2009.

[50] Paolo Giannozzi, Oliviero Andreussi, Thomas Brumme, Oana Bunau, Marco Buongiorno Nardelli, Matteo Calandra, Roberto Car, Carlo Cavazzoni, Davide Ceresoli, Matteo Cococcioni, et al. Advanced capabilities for materials modelling with Quantum ESPRESSO. *Journal of Physics: Condensed Matter*, 29(46):465901, 2017.

[51] Koichi Momma and Fujio Izumi. VESTA 3 for three-dimensional visualization of crystal, volumetric, and morphology data. *Journal of Applied Crystallography*, 44(6):1272–1276, 2011.

[52] B. G. Pfrommer, M. Cote, S. G. Louie, and M. L. Cohen. Relaxation of crystals with the quasi-Newton method. *Journal of Computational Physics*, 131:233–240, 1997.

[53] Dong C. Liu and Jorge Nocedal. On the limited-memory BFGS method for large-scale optimization. *Mathematical Programming*, 45(1–3):503–528, 1989.

[54] John P. Perdew, Kieron Burke, and Matthias Ernzerhof. Generalized gradient approximation made simple. *Physical Review Letters*, 77(18):3865, 1996.

[55] Georg Kresse and Daniel Joubert. From ultrasoft pseudopotentials to the projector augmented-wave method. *Physical Review B*, 59(3):1758, 1999.

[56] Hendrik J. Monkhorst and James D. Pack. Special points for brillouin-zone integrations. *Physical Review B*, 13(12):5188, 1976.

[57] Stefan Grimme, Jens Antony, Stephan Ehrlich, and Helge Krieg. A consistent and accurate *Ab Initio* parametrization of density functional dispersion correction (DFT-D) for the 94 elements H–Pu. *The Journal of Chemical Physics*, 132(15), 2010.

[58] Volker L. Deringer, Andrei L. Tchougréeff, and Richard Dronskowski. Crystal orbital hamilton population (COHP) analysis as projected from plane-wave basis sets. *The Journal of Physical Chemistry A*, 115(21):5461–5466, 2011.

- [59] Stefan Maintz, Volker L. Deringer, Andrei L. Tchougréeff, and Richard Dronskowski. Analytic projection from plane-wave and PAW wavefunctions and application to chemical-bonding analysis in solids. *Journal of Computational Chemistry*, 34(29):2557–2567, 2013.
- [60] Stefan Maintz, Volker L. Deringer, Andrei L. Tchougréeff, and Richard Dronskowski. LOBSTER: A tool to extract chemical bonding from plane-wave-based DFT. *Journal of Computational Chemistry*, 37:1030–1035, 2016.
- [61] Per-Olov Löwdin. On the non-orthogonality problem connected with the use of atomic wave functions in the theory of molecules and crystals. *The Journal of Chemical Physics*, 18(3):365–375, 1950.
- [62] Wei Tang, Eric Sanville, and Gustavo Henkelman. A grid-based bader analysis algorithm without lattice bias. *Journal of Physics: Condensed Matter*, 21(8):084204, 2009.